

Fast conversion and controlled deposition of lithium (poly)sulfides in lithium-sulfur batteries using high-loading cobalt single atoms



Yuanjian Li^{a,1}, Jiabin Wu^{a,1}, Bao Zhang^{b,1}, Wenyu Wang^a, Guoqun Zhang^a, Zhi Wei Seh^c, Nian Zhang^d, Jie Sun^e, Liang Huang^{a,**}, Jianjun Jiang^b, Jun Zhou^a, Yongming Sun^{a,*}

^a Wuhan National Laboratory for Optoelectronics, Huazhong University of Science and Technology, Wuhan, Hubei, 430074, PR China

^b School of Optical and Electronic Information, Huazhong University of Science and Technology, Wuhan, Hubei, 430074, PR China

^c Institute of Materials Research and Engineering, Agency for Science, Technology and Research (A*STAR), 2 Fusionopolis Way, Innovis, 138634, Singapore

^d Shanghai Institute of Microsystem and Information Technology, Chinese Academy of Sciences, Shanghai, 200050, PR China

^e School of Chemical Engineering and Technology, Tianjin University, Tianjin, 300072, PR China

ARTICLE INFO

Keywords:

Cobalt single atom
Lithium-sulfur batteries
Polysulfide redox reaction
Catalytic oxidation
Deposition of lithium sulfides

ABSTRACT

Lithium-sulfur (Li-S) batteries are appealing energy storage technologies owing to their exceptional energy density. Their practical applications, however, are largely compromised by poor cycling stability and rate capability because of detrimental shuttling of polysulfide intermediates, complicated multiphase sulfur redox reactions, and uncontrolled precipitation of the discharge products (lithium sulfide, Li₂S). Herein, monodispersed Co single-atom catalyst on conductive nitrogen-doped carbon nanosheet (CoSA-N-C) with high Co content of 15.3 wt% was fabricated through a salt-template method and used as a sulfur host material to simultaneously alleviate the polysulfide shuttling, propel the redox kinetics of dissolved polysulfides, and mediate the deposition of Li₂S. The robust two-dimensional architecture of CoSA-N-C with large surface area, high porosity, and dual lithiophilic-sulfiphilic Co-N species enable strong physical and chemical polysulfides confinement and fast electrons/ions transfer process. The densely populated Co-N₄ coordinated moieties function as electrocatalytic sites to accelerate the reversible conversion between lithium polysulfides and Li₂S. Importantly, the CoSA-N-C enables spatially controlled deposition of Li₂S nanoparticles during the battery discharge process, as opposed to conventional Li₂S passivation layers that fully covered the conductive host. Consequently, the as-fabricated cathodes based on the CoSA-N-C deliver high sulfur utilization (1574 mAh·g⁻¹ at 0.05 C), outstanding rate capability (624 mAh g⁻¹ at 5 C) and superior long-term stability (capacity fade rate of 0.035% per cycle for 1000 cycles at 1 C). Even under a sulfur loading up to 4.9 mg cm⁻², the reversible areal capacity could reach 4.24 mAh cm⁻² after 120 cycles at 0.2 C, delivering an ultrahigh capacity retention of 91.8%. This work sheds inspiring insights on the important role of single atomic metal with high mass loading in mediating the deposition of lithium sulfides and accelerating the reversible conversion of lithium polysulfides toward decent-performance Li-S batteries.

1. Introduction

The development of energy storage/conversion devices with high specific energies and long cycle longevity is one of the most desirable routes to meet the ever-expanding energy markets for various applications, including electric vehicles, grid-scale energy storage and wearable devices [1–4]. Among various electrochemical energy storage systems, lithium-sulfur (Li-S) battery has been recognized as one of the most appealing choices in terms of its exceptional theoretical energy density

(2600 Wh kg⁻¹) and abundant resources of sulfur [5–8]. Nevertheless, multiple drawbacks impede the implementation of Li-S batteries, including poor electrical/ionic conducting properties of active sulfur and lithium sulfide (Li₂S), drastic volumetric change (about 80%), and undesirable shuttling of soluble lithium polysulfide (LiPSs) intermediates during cycling [9–11]. These issues inevitably reduce the active sulfur utilization, cause rapid capacity fading, and induce poor rate capability, especially for cathode with high mass loading.

In an effort to tackle the foregoing drawbacks, extensive studies have

* Corresponding author.

** Corresponding author.

E-mail addresses: huangliang421@hust.edu.cn (L. Huang), yongmingsun@hust.edu.cn (Y. Sun).

¹ These authors contributed equally to this work.

been conducted and great research progress has been achieved by diverse designs of advanced electrode materials [12], separator [13–15], binder [16,17], and electrolyte [18,19]. Up to now, miscellaneous carbonaceous materials have been widely proposed to encapsulate active sulfur, since they are able to promote the electronic conductivity of cathode materials and offer physical confinement of polysulfides [20–22]. Unfortunately, the weak van der Waals force between nonpolar carbon materials and polar LiPSs molecules fails to fully prevent the leakage of soluble LiPSs intermediates and causes irreversible loss of active materials during long-term cycling. Polar transition metal oxides (e.g., TiO_2 and MnO_2) can work as polysulfide immobilizers via electrostatic or chemical interaction and mitigate the loss of active polysulfide species [23–25]. Nevertheless, these semiconducting metal oxides often have poor electronic conductivity, which is detrimental to the reduction kinetics from LiPSs to Li_2S during the discharge process and vice versa [26–28]. The sluggish conversion of polysulfide intermediates would cause their accumulation at the cathode side, and consequently their spontaneous migration from the cathode toward the anode. Furthermore, the LiPSs flooding also gives rise to uncontrolled precipitation of Li_2S passivation layer on the cathode surface that is generally hard to be fully reoxidized in the subsequent charge process due to its high decomposition barrier [29–31]. Therefore, rational design of metallic and polar host materials for sulfur cathodes that enable simultaneous entrapment and conversion of LiPSs may hold promise for restraining polysulfide shuttling and boosting the electrochemical performance of Li–S batteries.

Recently, metallic polar materials (e.g., Pt, Mo, CoS_2 , CoP, and MgB_2) [32–37] have shown electrocatalytic ability to improve the conversion kinetics between the solid (S_8 , Li_2S) and liquid (polysulfides) sulfur species in working Li–S batteries. Among these functional materials,

single metal atoms, usually loaded on high-surface-area conductive matrices, have received great attention due to their unique size quantum effect, unique electronic property, maximum atomic utilization, as well as unsaturated metal sites [38,39]. As a typical example, cobalt single atoms in nitrogen-doped graphene framework with available Co–N–C coordination centers were highly effective for promoting the reversible transformation between soluble LiPSs and insoluble Li_2S during charge/discharge process [40]. Iron single atoms on porous nitrogen-doped carbon [41–43] have also been employed as host materials to boost the anchorage and conversion of polysulfides. Moreover, the incorporation of single metal atoms (e.g., Fe, Co, Ni) on separator could reduce polysulfides crossover and accelerate their redox kinetics [44–49]. Despite these substantial progress, two major limitations still exist for the further development and utilization of single metal atoms in Li–S batteries: (1) Single metal atoms are often stabilized on host materials with physical or chemical bonds. The reported proportion of single metal atoms on host materials is very low (usually $< 5 \text{ wt}\%$) [40–46]. To optimize the battery performance, it is desirable to use materials containing a high content of single metal atoms, which provide a large number of active sites to achieve overall polysulfides immobilization and transformation efficiency [50,51]. (2) The effect of single metal atoms on the reversible deposition/dissolution of lithium sulfides is still unclear, which significantly affects the sulfur utilization and the electrochemical cycling of Li–S batteries [11,30,49,52].

Herein, monodispersed Co single atoms embedded in nitrogen-doped carbon nanosheets with up to 15.3 wt% Co content (CoSA-N-C) are synthesized through a salt-template method (Fig. 1a). Our experiments and theoretical calculations verify the advantages of CoSA-N-C as the sulfur host material (Fig. 1b): (1) Its large surface area enables high mass

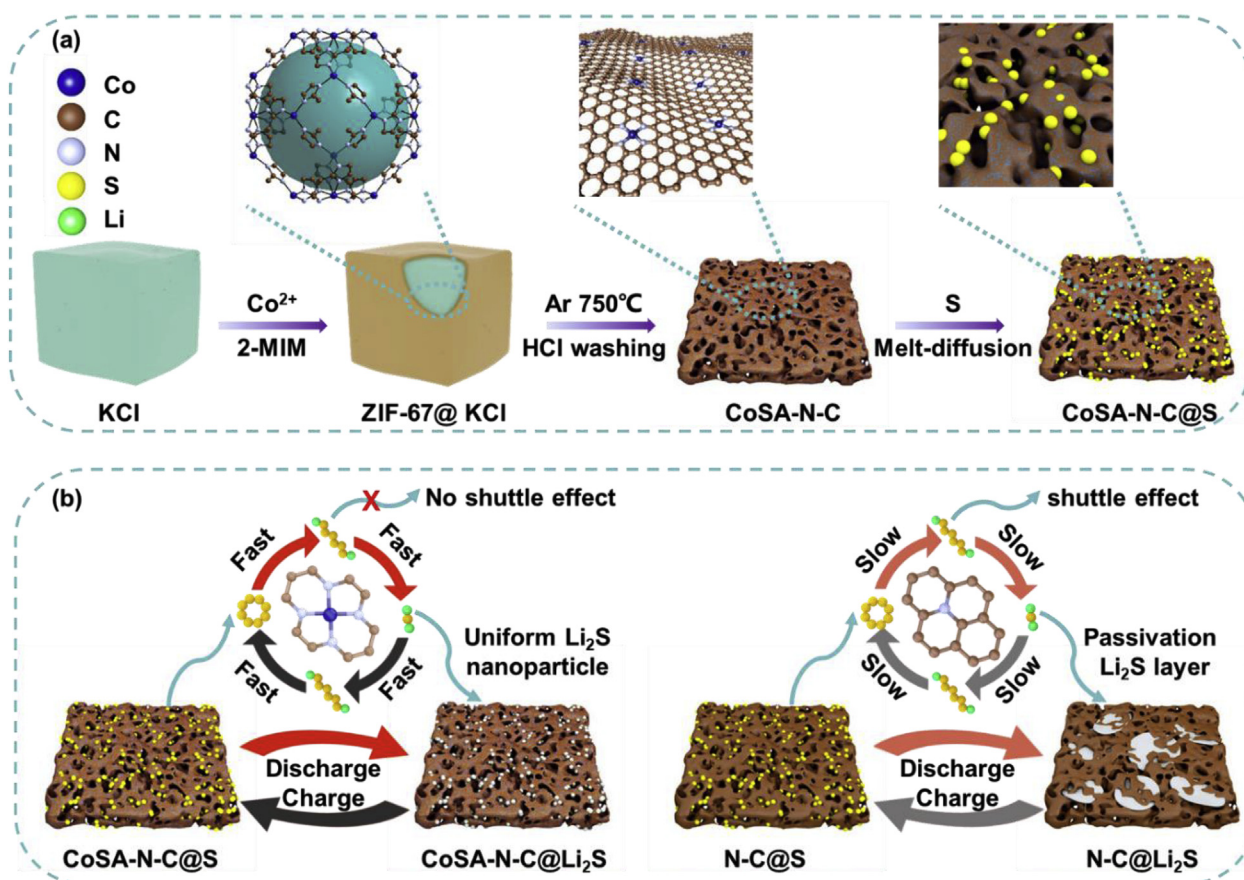


Fig. 1. Schematic illustration of the synthesis and application of the CoSA-N-C materials in Li–S batteries. (a) Schematic illustrations of the fabrication of CoSA-N-C and CoSA-N-C@S composite. (b) Schematic illustration of the effect of CoSA-N-C in improving the conversion kinetics between the solid (S, Li_2S) and liquid (polysulfides), and mediating the deposition of lithium sulfide nanoparticles.

loading of sulfur (74.2 wt%) and high conductivity allows fast ion/mass transfer during the electrochemical process. (2) A large number of Co single atoms offer adequate sulphophilic sites for the interaction with polysulfide anions and the N dopants bind the terminal Li in LiPSs molecules, which contributes to strong chemisorption of CoSA-N-C host for sulfur species during charge/discharge process. (3) The coordination between Co sites and surrounding N sites in the form of atomic Co–N₄ structure not only accelerates polysulfide conversion, but also reduces the kinetic barrier of Li₂S oxidation, which propels the redox kinetics of sulfur chemistry in Li–S batteries. (4) CoSA-N-C regulates the deposition of Li₂S nanoparticles instead of forming a passivated Li₂S layer on the entire surface of the electrode, which helps to maintain high conductivity and high sulfur utilization during cycling. Consequently, the fabricated CoSA-N-C electrode displays superior electrochemical performance featuring a large specific capacity of 1574 mAh·g⁻¹ at 0.05 C, a small fading rate of 0.035% per cycle for 1000 cycles at 1 C, an enhanced rate capability of 624 mAh g⁻¹ at 5 C, concurrently with a satisfied capacity retention of 91.8% after 120 cycles at 0.2 C with a sulfur loading of 4.9 mg cm⁻², demonstrating great promise for scale implementation in high energy Li–S batteries.

2. Results and discussion

The CoSA-N-C material was fabricated by a reported salt-template

strategy [53], as illustrated in Fig. 1a. It starts from the growth of cobalt zeolitic imidazolate frameworks (ZIF-67) on the surface of potassium chloride (KCl) particles via the coordination of cobalt (II) precursor and 2-methylimidazole (2-MIM) at 70 °C. Upon annealing the ZIF-67@KCl precursor under an argon atmosphere at 750 °C for 2 h and subsequently rinsing in hydrochloric acid solution, the final CoSA-N-C product could be obtained. Notably, the inductively coupled plasma optical emission spectrometry (ICP-OES) measurement determines that Co content in the CoSA-N-C reaches as high as 15.3 wt%, which is consistent with the thermogravimetric analysis (TGA, Fig. S1). This value is surprisingly higher than previously reported SACs for Li–S batteries (Table S1). It is recognized that the salt-template is responsible for the formation of high metal loading of CoSA-N-C. In particular, the KCl template could prevent the large shrinkage of the thin ZIF-67 layer during high temperatures pyrolysis, therefore achieving densely dispersed Co atoms and Co–N species that are immobilized on the ultrathin carbon supports. For control experiments, a metal-free nitrogen-doped carbon nanosheet (NC) was prepared by the zinc-based ZIF (ZIF-8@KCl) precursor under the same conditions (Fig. S2).

The morphology of CoSA-N-C was studied using transmission electron microscopy (TEM) (Fig. 2a). It can be observed that the as-synthesized CoSA-N-C has a 2D sheet-like morphology with wrinkled surface. The thickness of CoSA-N-C nanosheet is found to be around 1.4 nm via atomic force microscopy (AFM) measurement (Fig. S3), illustrating their

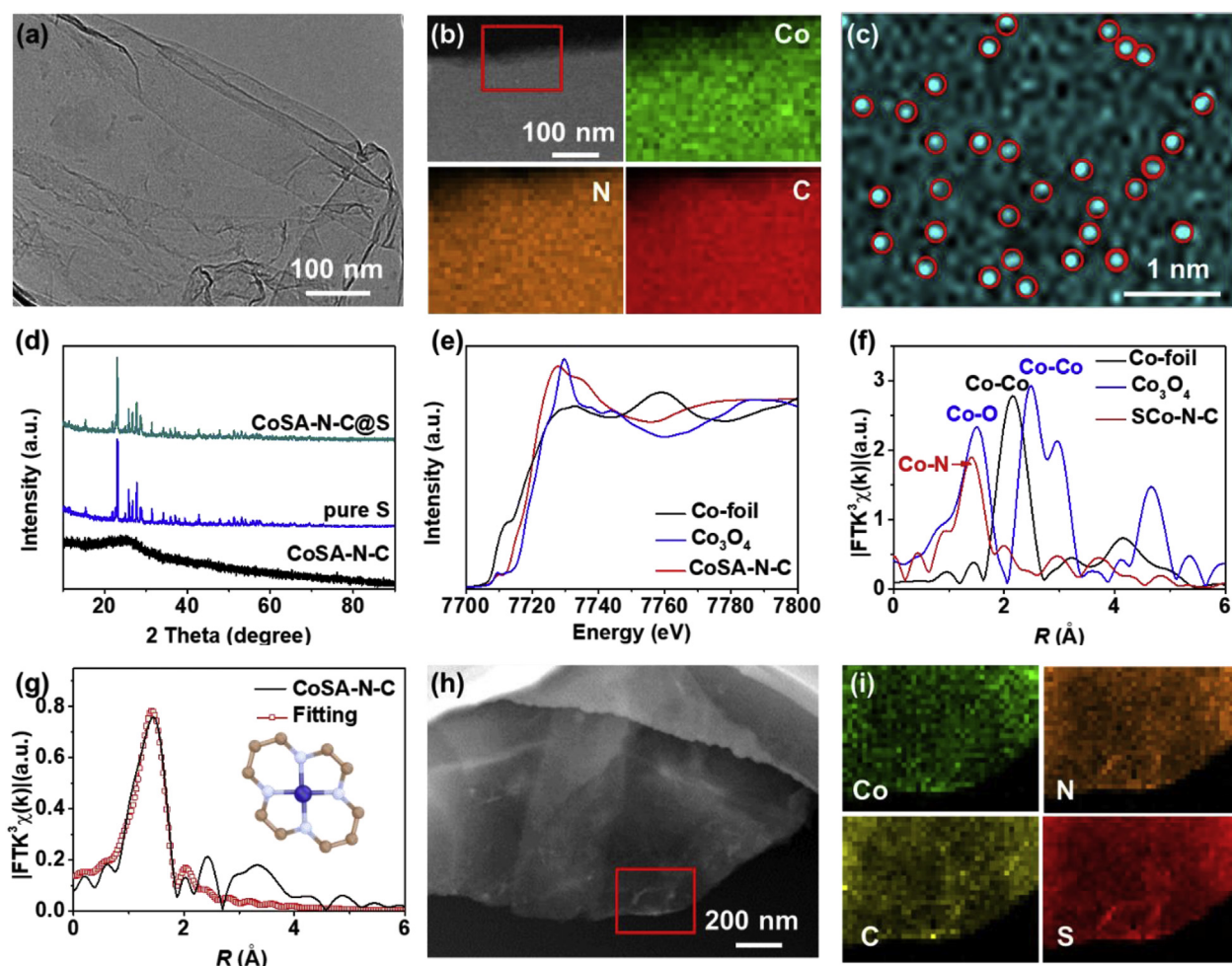


Fig. 2. Characterizations of CoSA-N-C and CoSA-N-C@S composite. (a) TEM and (b) corresponding EDX elemental mapping images of CoSA-N-C. (c) HAADF-STEM image of CoSA-N-C, where the bright dots were Co atoms (circled in red for better observation). (d) XRD patterns of CoSA-N-C, pure S, and CoSA-N-C@S composite. (e) XANES and (f) FT-EXAFS spectra of Co₃O₄, Co foil, and CoSA-N-C. (g) The corresponding EXAFS fitting curves of CoSA-N-C. The inset shows the depicted Co–N₄ structure. (h) TEM and (i) corresponding elemental mapping images of CoSA-N-C@S. (For interpretation of the references to color in this figure legend, the reader is referred to the Web version of this article.)

ultrathin features. The energy dispersive X-ray (EDX) mapping images of CoSA-N-C are displayed in Fig. 2b, where a homogeneous distribution of C, N, and Co elements in the sample can be seen. The existing form of cobalt atoms was then visualized by aberration-corrected high-angle annular dark-field scanning transmission electron microscopy (HAADF-STEM). As depicted in Fig. 2c, the observed numerous bright dots in subangstrom size (circled in red for better observation) are corresponding to Co single sites, which randomly disperses in the carbon support. No obvious cobalt-containing nanoparticles or clusters could be detected in the X-ray diffraction patterns (XRD, Fig. 2d) and scanning electron microscopy images (SEM, Fig. S4).

X-ray photoelectron spectroscopy (XPS) survey spectrum of CoSA-N-C indicates the co-existence of C, N, Co, and O elements (Fig. S5a). The atomic ratio of N is ~16.3%, suggesting a N-rich surface of CoSA-N-C host, which is expected to promote surface electron transfer and improve chemical affinity toward polysulfides [54,55]. The deconvoluted N 1s spectrum is displayed in Fig. S5b, showing three characteristic peaks at 398.5, 400.3, and 401.6 eV, which are resolved into pyridinic N, pyrrolic N, and graphitic N, respectively. Obviously, the dominant N configurations in the CoSA-N-C composite are pyridinic and pyrrolic N, which are normally considered to coordinate metal atoms through chemical bonding [41, 47]. The high-resolution Co 2p spectrum (Fig. S5c) exhibits typical Co 2p_{3/2} and 2p_{1/2} peaks at 781.2 and 796.5 eV, respectively. X-ray absorption near-edge structure (XANES) and extended X-ray absorption fine structure (EXAFS) measurements were conducted to further study local coordination structure and the chemical state of these Co atoms. The results for CoSA-N-C are presented concurrently with those for Co foil and Co₃O₄ as references. The XANES profiles (Fig. 2e) show the pre-edge peak of CoSA-N-C located between those of Co foil (Co⁰) and Co₃O₄ (Co²⁺, Co³⁺), suggesting that centered Co atoms in CoSA-N-C are positively charged [41]. In the EXAFS spectra (Fig. 2f), the main peak of CoSA-N-C is located at 1.41 Å, which can be assigned to the Co–N scattering paths. In the meantime, no obvious Co–Co peak at about 2.16 Å is observed. Furthermore, EXAFS fitting results (Fig. 2g) indicate a four-coordination mode of Co–N in the CoSA-N-C [53]. Therefore, we believe that Co atoms are coordinated with N atoms to form Co–N₄ moieties, which are atomically dispersed in CoSA-N-C on the basis of TEM and XAFS analyses.

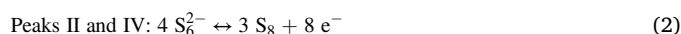
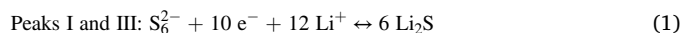
Raman spectrum of CoSA-N-C composite in Fig. S6 presents two typical D (1355 cm⁻¹) and G (1585 cm⁻¹) bands with an intensity ratio of 1.06, which evidences a graphitic carbon nature of the prepared CoSA-N-C. Such highly graphitized structure benefits from the catalytic effect of cobalt during carbonization and provides high conductivity for fast electron transfer. To further investigate the porosity of CoSA-N-C, N₂ adsorption-desorption analysis was performed (Fig. S7). The Brunauer-Emmett-Teller (BET) specific surface area and total pore volume are measured to be 403.8 m² g⁻¹ and 0.49 cm³ g⁻¹, respectively, which are slightly smaller than those of the N–C sample (490.8 m² g⁻¹ and 0.70 cm³ g⁻¹). In addition, the Barrett-Joyner-Halenda pore size distributions demonstrate the co-presence of micropores with diameters of ~1.6 nm and mesopores from 4 to 25 nm in size. The large surface area and hierarchical meso-microporous architecture bring multiple benefits for guaranteeing high sulfur loading, well-accommodated volume expansion, and efficient physical confinement of polysulfides. Together with the sufficient electrochemically active sites, the prepared CoSA-N-C can be a promising sulfur host.

Through a conventional melt-impregnation method, a high quantity of elemental sulfur was impregnated into CoSA-N-C host. The TGA analysis (Fig. S8) shows a high sulfur mass content of 74.2% in CoSA-N-C@S composite. XRD pattern of obtained CoSA-N-C@S composite (Fig. 2d) indicates successful incorporation of sulfur, the characteristic diffraction peaks can be indexed to orthorhombic sulfur. After loaded with sulfur, CoSA-N-C@S composite also exhibits a sharply decreased specific surface area (21.5 cm² g⁻¹) and overall pore volume (0.036 cm³ g⁻¹). From the TEM image in Fig. 2h, we can see that CoSA-N-C@S composite still maintains the nanosheet structure of CoSA-N-C. The

corresponding elemental mapping images in Fig. 2i reveal that all the elements of Co, N, C, and S are evenly dispersed in the CoSA-N-C@S composite, a reflection of the uniform coverage of sulfur on the well-designed CoSA-N-C nanosheet.

It is well-known that the adsorption ability of sulfur hosts plays an essential role in immobilizing LiPSs in the cathode side and therefore improving cell performance. To probe the affinity of CoSA-N-C with sulfur species, a solution of 0.1 M Li₂S₆ in a mixture of dioxolane/dimethoxyethane (DOL/DME, 1:1 in volume) was prepared for polysulfide adsorption tests. The resulting photographs in Fig. 3a exhibit that the Li₂S₆ solution with the addition of CoSA-N-C becomes nearly colorless after 6 h of adsorption, however, the solution mixed with N–C shows only slight color change. This sharp color change in the former case emphasizes the strong absorbing capabilities of CoSA-N-C for Li₂S₆ species, which is further supported by XPS analysis. The detected S 2p spectrum (Fig. 3b) after the adsorption test exhibits three contributions at 162.7/163.7, 163.3/164.7, and 167.0/168.2 eV, representing the terminal (S_T⁻¹), bridged sulfur (S_B⁰) atoms, and thiosulfate species respectively. The formation of thiosulfate is associated with the surface redox reaction between Li₂S₆ ions and CoSA-N-C composite [56,57]. With respect to the previous reference, the binding energies of S_T⁻¹ in our case shift to higher values by 1.0 eV, close to more covalent S_T-Co bond, which indicates the electron transfer from Li₂S₆ to the Co centers in CoSA-N-C [58,59]. Meanwhile, the Co 2p peaks of CoSA-N-C upon contact with Li₂S₆ downshifts (Fig. S5b), which further sheds light on the interaction between Co atoms and polysulfide ions. On the other hand, the Li 1s spectrum (Fig. 3c) of CoSA-N-C/Li₂S₆ exhibits a peak at 168.2 eV that belongs to the Li–N bond, suggesting the strong chemical bonding between active N sites in CoSA-N-C and the terminal Li in Li₂S₆. The Li–N interaction is also validated in N 1s spectrum (Fig. S5c), as the binding energies of N species of CoSA-N-C/Li₂S₆ are higher in comparison with those of pristine CoSA-N-C. We further studied the underlying principles of the adsorption behavior of CoSA-N-C by density functional theory (DFT) calculations. The optimal configurations presented in Fig. 3d–f depict the adsorption for Li₂S₆ on the metal sites and N dopants in CoSA-N-C with an adsorption energy of –0.50 and –0.35 eV, respectively, which are much stronger than that on N dopants in N–C (–0.12 eV), further indicating the excellent adsorption strength of LiPSs species by CoSA-N-C. Combining results from adsorption experiment, XPS analysis, and DFT conclusions, it can be concluded that, in CoSA-N-C, the Co and N atoms act as dual lithiophilic-sulfiphilic sites, which is beneficial to adsorb LiPSs and mitigate their dissolution and shuttling behavior during cell operation.

Besides the advantages of strong adsorption of polysulfides, catalyzing their fast conversion to the insoluble discharging/charging products of Li₂S/S₈ is also necessary to realize high-rate Li–S batteries. To elucidate the superiority of CoSA-N-C in improving the liquid-solid transformation, the kinetics of redox reactions was systemically investigated via cyclic voltammograms (CVs) in a symmetric cell, which use two catalysts as identical working and counter electrodes and 0.5 M Li₂S₆ as electrolyte. As exhibited in Fig. 4a, the CV curve of CoSA-N-C symmetric battery exhibits high reversibility with four distinct reduction/oxidation peaks centered at –0.382 (Peak I), –0.025 (peak II), 0.177 (peak III), and 0.025 V (peak IV). These peaks are related to the following forward and reverse electrochemical reactions of Li₂S₆, respectively [60,61],



The CV of symmetric battery with N–C electrode otherwise exhibits only one pair of feeble and wide peaks with a serious voltage separation, illustrating slow reaction kinetics and poor redox charge storage. The CoSA-N-C symmetric battery without the addition of Li₂S₆ is also compared and the corresponding CV curve presents rectangular shape and negligible current response that points out the capacitive behavior of CoSA-N-C. Meanwhile, the Nyquist plots in the electrochemical

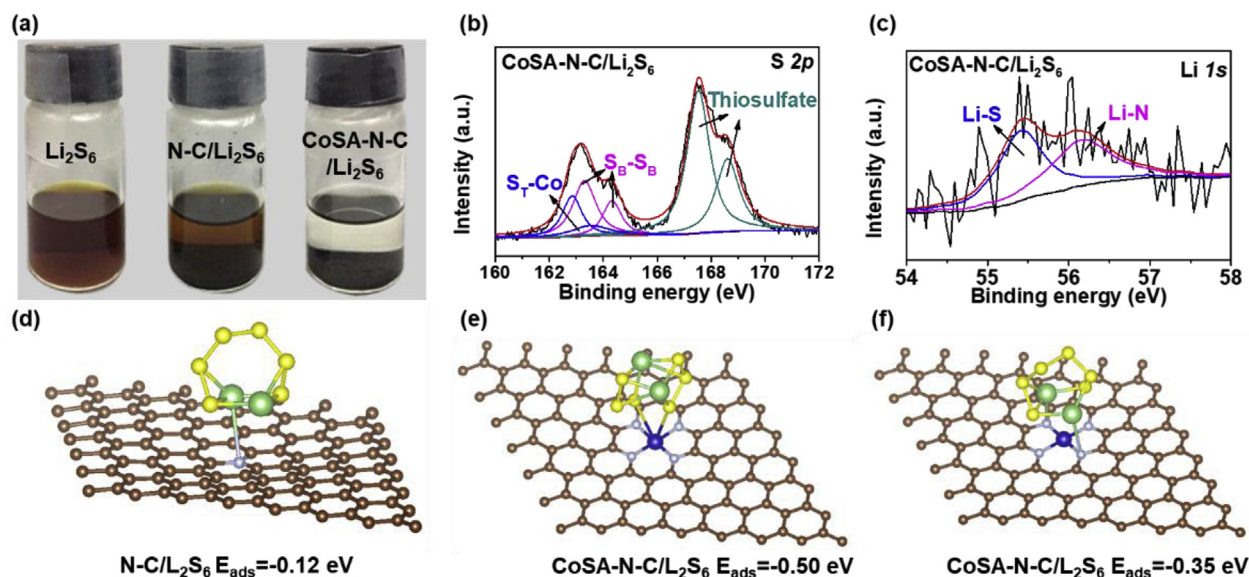


Fig. 3. Adsorption behavior of polysulfides on CoSA-N-C host. (a) Digital images of solutions containing 0.1 M Li_2S_6 dissolved in a mixture of DOL/DME (1:1 in volume) after contacting with CoSA-N-C and N-C for 6 h. High-resolution XPS spectra of (b) S 2p and (c) Li 1s of the obtained CoSA-N-C/ Li_2S_6 . (d–f) Atomic conformations and binding energy for Li_2S_6 species adsorption on N-C and CoSA-N-C based on DFT calculations. Here, the brown, yellow, green, white, and blue balls represent C, S, Li, N, and Co atoms, respectively. (For interpretation of the references to color in this figure legend, the reader is referred to the Web version of this article.)

impedance spectroscopy (EIS) of symmetrical cells (Fig. 4b) reveal that CoSA-N-C electrode depicts half the charge transfer resistance (R_{ct}) of N-C (7.4 vs. 15.1 Ω), manifesting high electrical conductivity of CoSA-N-C and favorable charge and ion transfer kinetics at CoSA-N-C/LiPSs interface [61,62]. Lithium-catalyst cells were employed to further validate the effectiveness of CoSA-N-C in polysulfide catalysis. The oxidation of polysulfide to sulfur was monitored following a potentiostatic charging from the open circuit condition to 2.4 V [62,63], as displayed in Fig. 4c. The earlier appearance of the nucleation peak along with the increased peak intensity of CoSA-N-C than N-C reveals the rapid kinetics of promoting solid sulfur deposition on CoSA-N-C hosts. The reduction kinetics of polysulfide to lithium sulfide was examined likewise by the potentiostatic discharge experiment (Fig. 4d) [62,63]. Similarly, the larger Li_2S nucleation peak occurs again on the CoSA-N-C electrode, suggesting an improvement of the Li_2S precipitation kinetics. The above experiment results clearly confirm that the CoSA-N-C cathode host possesses facile kinetics of the liquid-solid conversion from dissolved Li_2S_6 to insoluble S and Li_2S .

The electrocatalytic effect of CoSA-N-C host on the sulfur transformation chemistry is further investigated in actual Li-S coin cells using a CoSA-N-C@S cathode and a lithium metal anode. Fig. 4e exhibits the CV curves of the Li-S cells with the two kinds of cathodes recorded at a low scan rate of 0.2 mV s^{-1} . For the CoSA-N-C@S cathode, the two well-defined cathodic peaks at 2.31 (peak C1) and 2.03 V (peak C2) are ascribed to the reduction of solid-state sulfur to soluble LiPSs intermediates (Li_2S_x , $4 \leq x \leq 8$) and subsequently to insoluble Li_2S , while the major anodic peak at 2.37 V (peak A) stems from the reconversion of Li_2S to LiPSs and eventually to sulfur [10]. In contrast, those cathodic/anodic peaks on the N-C@S counterpart shift to the more negative/positive position respectively in the CV curves, implying an increase of cell polarization. The potential shift also suggests that the CoSA-N-C can trigger rapid solid-liquid and liquid-solid conversions during Li-S cell operation. The function of the CoSA-N-C was further investigated by analyzing the Tafel plots (Fig. 4f) [64,65]. Likewise, CoSA-N-C@S cathode shows smaller Tafel slopes compared with the case of N-C@S cell at all three charge and discharge plateaus (Table S2), which implies rapid polysulfide redox conversion, favorable Li_2S deposition, and fast Li_2S oxidation on the surface of CoSA-N-C@S cathode.

Thus, the above CV results prove that the CoSA-N-C host effectively triggers promoted kinetics of round-trip redox reactions ($\text{S}_8 \leftrightarrow \text{S}_6^{2-} \leftrightarrow \text{Li}_2\text{S}$) in practical Li-S batteries.

Furthermore, CV tests under different scanning rates ranging from 0.2 to 0.5 mV s^{-1} were performed to study the Li^+ diffusion dynamics. The cathodic and anodic current peaks (I_{C1} , I_{C2} , I_A) have a linear relationship with the square root of scanning rates, illustrating the reaction is diffusion-limited (Fig. S9). Accordingly, the lithium-ion diffusion coefficient (D_{Li^+}) was calculated using the classical Randles-Sevcik equation [29,66]

$$I_p = (2.69 \times 10^5) n^{1.5} A D_{\text{Li}^+}^{0.5} C_{\text{Li}^+} \nu^{0.5} \quad (3)$$

where I_p is the peak current, n is the number of charge transfer ($n = 2$), S is the geometric electrode area ($S = 0.785 \text{ cm}^2$), D_{Li^+} is the lithium-ion diffusion coefficient, C_{Li^+} is the concentration of Li^+ in the cathode ($C = 0.001 \text{ mol cm}^{-3}$ based on 1 M LiTFSI), and ν is the scan rate. The calculated D_{Li^+} values are summarized in Fig. 4d. It can be unanimously noticed that the CoSA-N-C@S electrode delivers D_{Li^+} values of 1.99, 3.76, and $5.18 \times 10^{-8} \text{ cm}^2 \text{ s}^{-1}$ for peaks C1 and C2, and A, respectively, while the N-C@S electrode possesses D_{Li^+} values of 1.24, 1.63, and $3.33 \times 10^{-8} \text{ cm}^2 \text{ s}^{-1}$ for peaks C1 and C2, and A. The enhanced Li^+ diffusivity on CoSA-N-C@S cathode surface can be attributed to the Co-N₄ moieties on CoSA-N-C that favor adsorption and conversion of LiPSs, therefore, preventing deposition of an insulating layer on the cathode (as discussed below). Furthermore, the ultrathin and porous lamellar architecture of CoSA-N-C shortens the ion transport path, which can facilitate fast Li^+ transport.

Fig. 5a compares the initial discharge voltage profiles of the CoSA-N-C@S and N-C@S electrodes at a current rate of 0.05 C (1 C = 1675 mA g^{-1}), in which typical two-plateau behavior is observed, consistent with the above CV results. CoSA-N-C@S cathode contributes a capacity of 1574 mAh g^{-1} , which is very close (94%) to the theoretical capacity of sulfur (1675 mAh g^{-1}) and much better than that of N-C@S cathode (73%). To obtain in-depth information on the high sulfur utilization, the quantification analysis of high and low plateau discharge capacities (Q_H and Q_L) was conducted. In general, the higher plateau at 2.3 V represents the conversion of element S to long-chain LiPSs (Li_2S_x , $4 \leq x \leq 8$), while the lower discharge plateau at 2.1 V corresponds to the reduction of LiPSs

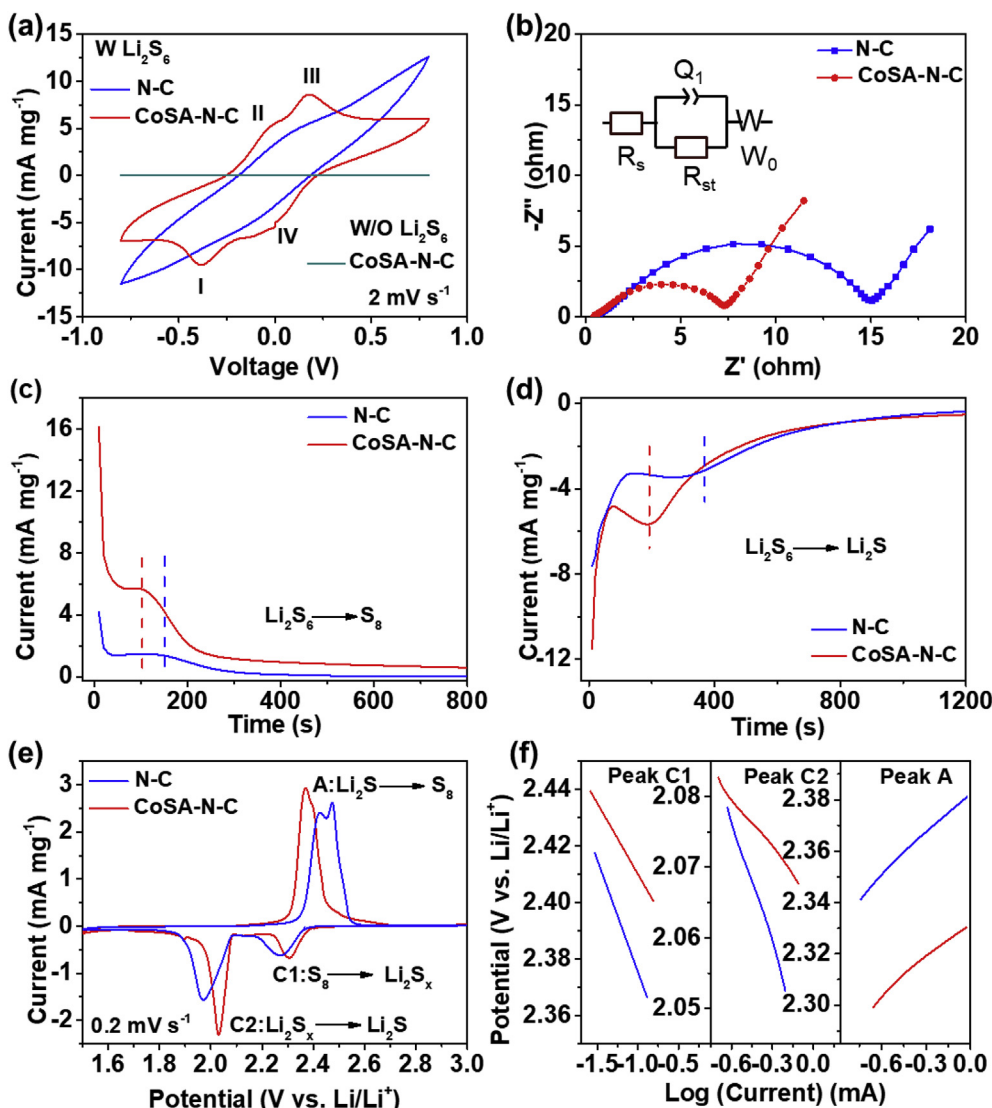


Fig. 4. Catalysis of polysulfides conversion on CoSA-N-C host. (a) CV profiles and (b) EIS spectra of the symmetrical cells with N-C and CoSA-N-C electrodes using an electrolyte containing 0.5 M Li₂S₆ and 1 M LiTFSI dissolved in DOL/DME (v/v = 1/1), respectively. Current-time plots of N-C and CoSA-N-C electrodes for (c) potentiostatic charging from the open circuit voltage (OCV, 2.2 V) to 2.4 V and (d) potentiostatic discharging from the OCV to 2 V. (e) CV profiles of Li-S coin cells with CoSA-N-C@S and N-C@S electrodes, respectively. (f) Tafel plots of CoSA-N-C@S and N-C@S electrodes for the first cathodic reduction process (Peak C1: S₈ → Li₂S_x, 4 ≤ x ≤ 8), second cathodic reduction process (Peak C2: Li₂S_x → Li₂S, 4 ≤ x ≤ 8), and anodic oxidation process (Peak A: Li₂S → S₈).

to insoluble Li₂S. Apart from the higher Q_H and Q_L, the CoSA-N-C@S cathode displays a larger Q_L/Q_H value of around 2.93 than that of S/NG (2.29). These findings provide strong evidence that CoSA-N-C is able to confine active intermediates within the cathode zone and promote liquid-solid transformation from LiPSs to Li₂S during the discharge process, and thus brings the high specific capacity of CoSA-N-C@S cathode (Fig. S10) [67,68]. At the end of discharge, the cells were disassembled to investigate the morphology of Li₂S precipitate. As exhibited in Fig. 5c and d, the corresponding SEM images illustrate that N-C@S cathode surfaces are covered by sparse and large Li₂S film, while dense Li₂S nanoparticles are observed on CoSA-N-C@S cathode surface. These observations indicate that the CoSA-N-C alter the growth mode of Li₂S precipitants from conventional discontinuous films to uniform nanoparticle, contributing to promoted polysulfides reduction as well as the high sulfur utilization [32,69]. Furthermore, the well-distributed Li₂S particles would significantly increase the interface with conductive networks and electrolyte, and account for the speedy electrons and ions transport, which promotes reutilization during the following charging process.

From the initial charge profiles in Fig. 5b, it can be found that the N-C@S electrode exhibits a high potential barrier at about 2.32 V, which could be ascribed to the ineffectiveness of N-C for catalyzing the oxidation of Li₂S. In the case of the CoSA-N-C@S cathode, the charge voltage plateau is significantly lower than 2.20 V, indicating the delithiation reaction of Li₂S can easily occur on the surface of CoSA-N-C. To

further anatomize the decomposition energy and barrier of Li₂S, the climbing-image nudged elastic band (CI-NEB) method was adopted [29]. The decomposition process from an intact Li₂S molecule into a LiS cluster is stated as a single Li-ion detaching from the Li₂S molecule (Li₂S → LiS + Li⁺ + e⁻), and the relative energy profiles are displayed shown in Fig. 5e and f. The calculated Li₂S decomposition barriers for CoSA-N-C/Li₂S and N-C/Li₂S are 1.08 and 1.48 eV, respectively, which qualitatively agree with our experimentally measured initial voltage barrier. The experiment and theoretical analysis demonstrates the synergic effect of CoSA-N-C catalyst in Li₂S oxidation. Therefore, we can conclude that dense Co-N₄ moieties on CoSA-N-C surface can strengthen the chemisorption of polysulfides, promote their conversion to Li₂S, achieve the uniform precipitation of Li₂S nanoparticle, and catalyze the Li₂S oxidation, which is the reason for lowering the energy barriers in whole-range Li-S redox reactions.

Having thoroughly investigated the effectiveness of CoSA-N-C as sulfur support for Li-S batteries, we went on to study their rate and cycle performances. Fig. 6a shows the electrochemical capacity of CoSA-N-C@S cathode at various current densities. It exhibits average specific capacities of 1307, 1088, 978, 883, and 829 mAh g⁻¹ at 0.1, 0.2, 0.5, 1, and 2 C, respectively. Even under a large current density of 5 C, a notable capacity of 624 mAh g⁻¹ is still retained, indicative of the ultrahigh rate capability of CoSA-N-C@S cathode. After switching the current density back to 0.2 C, the recovered capacity stabilizes at 1046 mAh g⁻¹,

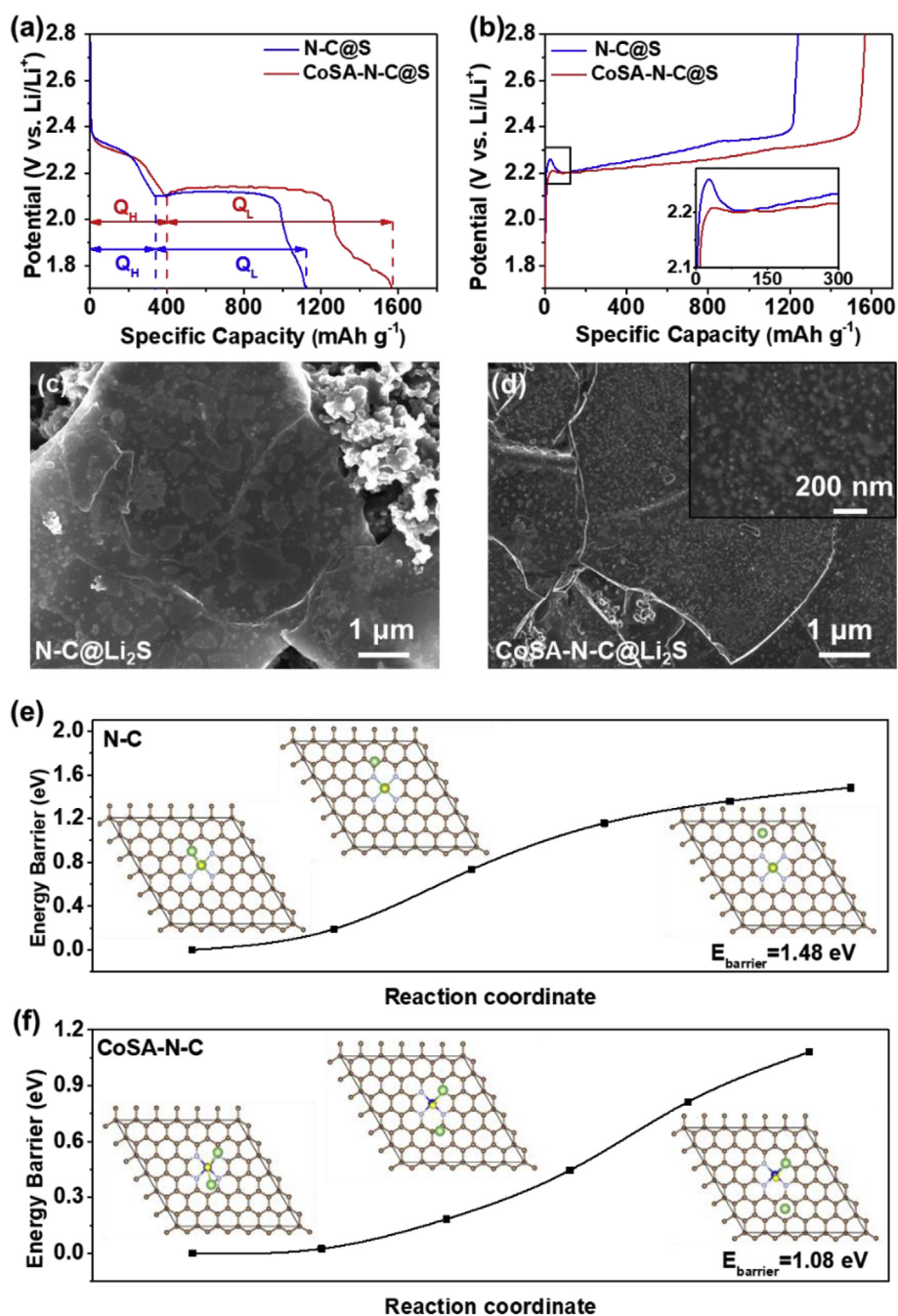


Fig. 5. Li₂S deposition and decomposition on CoSA-N-C host. (a) Initial discharge voltage profile of CoSA-N-C@S and N-C@S electrodes at 0.05 C. Q_H and Q_L represent the capacities of high and low discharge plateau, respectively. (b) Initial charge voltage profile of CoSA-N-C@S and N-C@S electrodes at 0.05 C. The inset is the enlarged view of the boxed areas. SEM images of Li₂S that deposits on (c) N-C and (d) CoSA-N-C electrodes at the end of initial discharge process. Energy profiles of the decomposition of a Li₂S cluster on (e) N-C and (f) CoSA-N-C. The brown, yellow, green, white, and blue balls represent C, S, Li, N, and Co atoms, respectively. (For interpretation of the references to color in this figure legend, the reader is referred to the Web version of this article.)

implying remarkable electrochemical reversibility. In contrast, the N-C@S cathode shows inferior performance, as featured by the rapidly decreased capacities from 1107 to 186 mAh g⁻¹ when the current rate stepwise ramps from 0.1 to 5 C. The corresponding charge/discharge curves at different current densities are displayed in Fig. 6b and Fig. S11. It shows that, the CoSA-N-C@S cathode maintains flat voltage plateaus on both the discharging and charging processes at each current rate, indicating a reduced electrochemical polarization with smaller potential gaps in comparison with the case of N-C@S cathode. EIS analysis was performed after the rate test to further reveal the electrochemical kinetics (Fig. 6c). The CoSA-N-C@S electrode exhibits smaller charge-transfer resistance (~9.8 Ω) than N-C@S electrode (~15 Ω), indicating a faster charge/mass transfer kinetics during lithiation/delithiation reaction. Consequently, the superior rate performance of CoSA-N-C@S is ascribed to dynamically propelled kinetics of whole-range Li-S redox reactions on

CoSA-N-C surface.

The cycling performances for different cathodes were evaluated by galvanostatic cycling at 0.5 C (Fig. S12). For the N-C@S cathode, it delivers an initial discharge capacity of 827 mAh g⁻¹ and drastically falls to 493 mAh g⁻¹ after 150 cycles. Surprisingly, the discharge capacity of CoSA-N-C@S cathode is as high as 1055 mAh g⁻¹ at the first cycle and is still kept at 871 mAh g⁻¹ after 150 cycles, corresponding to an impressive capacity retention of 83%. It is worth noting that the CoSA-N-C cell without S loading only delivers a negligible capacity under the same testing conditions (Fig. S13). To verify possible reasons that influence cycling stability, we examined the morphology and structure of the sulfur cathodes, separator, and Li anodes via disassembling the cells after 150 cycles. We note that the color of the DME solution after soaking the cycled CoSA-N-C@S and N-C@S cathodes is vastly different: the nearly colorless solution for the CoSA-N-C@S cathode suggests considerably

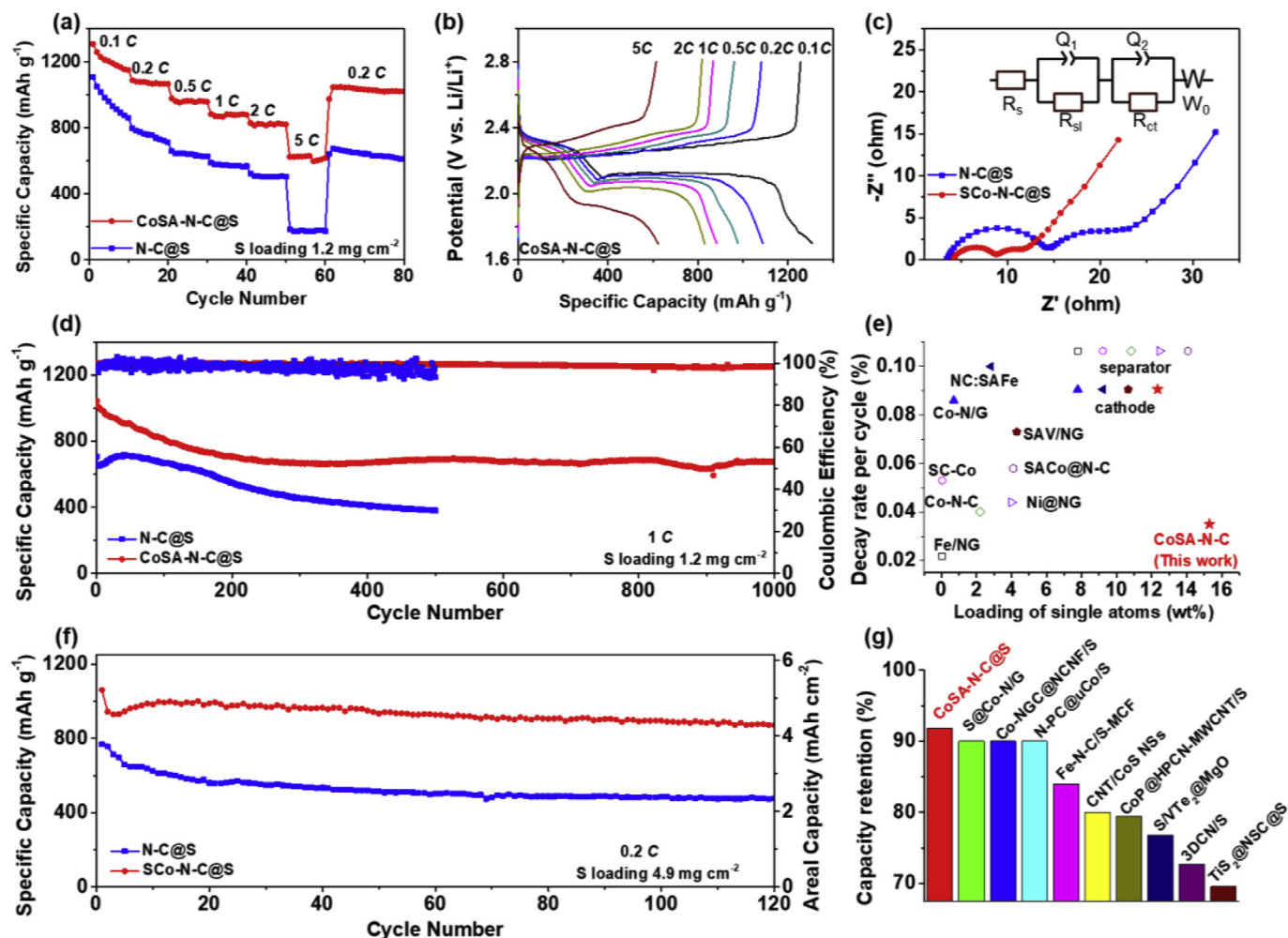


Fig. 6. Electrochemical performance of Li-S cells. (a) Rate performance of the CoSA-N-C@S and N-C@S cathodes at various C rates from 0.1 C to 5 C. (b) Discharge-charge curves of the CoSA-N-C@S cathodes at various current densities. (c) EIS spectra of the CoSA-N-C@S and N-C@S cathodes after rate test. (d) Long-term cycling performance of the CoSA-N-C@S and N-C@S cathodes at 1 C. (e) Performance comparisons with recent works on single-atoms catalysts-based cathode and separator in Li-S batteries for long-term cycling (>300 cycles). (f) Cycling performance of CoSA-N-C@S and N-C@S cathodes with S areal mass loadings of 4.9 mg cm⁻² at 0.2 C. (g) Performance comparisons with recent works on catalytic cathodes with high S mass loading (>3.5 mg cm⁻²).

restricted polysulfide dissolution (Fig. S14). Meanwhile, the Li anode and separator from the CoSA-N-C@S cell also exhibit much lighter color than those from the N-C@S cell, further confirming superior inhibition of CoSA-N-C on polysulfide shuttling upon cycling. Furthermore, the shape and structure of the CoSA-N-C@S cathode can be well conserved after hundreds of cycles (Fig. S15). Meanwhile, the structural integrity of Li electrode is well-preserved after cycling with the CoSA-N-C@S cathode, but the cycled Li anode coupled with N-C cathode displays a looser and rougher surface with obvious cracks (Fig. S16). Thus, we conclude that the CoSA-N-C host with Co-N₄ moieties greatly suppresses polysulfide shuttling and simultaneously retards the detrimental reaction with the metal lithium, which thus accounts for extraordinary cycling performance.

To meet the requirements for commercialization, we further examined the long-term cycling stability of the CoSA-N-C@S cathode at a high rate of 1 C. As exhibited in Fig. 6d and S17, after 1000 cycles, the cathode maintains high reversible capacity of 675 mAh g⁻¹ with a small capacity fading rate per cycle of 0.035% and high Coulombic efficiency of 99.5%. The stable cycling performance is superior to most of the previous reported catalytic sulfur cathodes (Table S3). The comparison of the present work with other reported single-atoms catalysts as cathode and separator materials in Li-S batteries are also displayed in Fig. 6e. Our result is among the best to date (details in Table S1), strongly

highlighting the advantages of the single-atoms catalyst with high-metal loading for rechargeable Li-S batteries. As a contrast, the N-C/S cathode yields a comparatively low specific capacity of 381 mAh g⁻¹ after only 500 cycles (capacity degradation rate of 0.092% per cycle) and suffers from a low Coulombic efficiency (average about 97.1%). Improving the areal sulfur loading is imperative for high-energy-density Li-S batteries. Under a high areal loading of 4.9 mg cm⁻² and a low electrolyte/sulfur ratio of 10.4 μL mgS⁻¹, the CoSA-N-C@S cathode contributes a high specific discharge capacity of 1061.7 mAh g⁻¹ at 0.2 C, which corresponds to an areal capacity of 4.63 mAh cm⁻² (Figs. 6f and S19). Under such sulfur mass loading and areal capacity, the gravimetric energy density of CoSA-N-C based Li-S battery is 163.3 Wh kg⁻¹ at a system level considering the total mass of the cathode, electrolyte, separator, and Li metal (see details in Table S4). Further improvement can be achieved by the optimization at the cell level, such as reducing the amount of electrolyte in a pouch cell configuration. After 120 cycles, the areal capacity remains at 4.24 mAh cm⁻² (specific capacity of 871.3 mAh g⁻¹), delivering a high capacity retention of 91.8%, which is considerably larger than N-C@S cathode (61.9%) and many other advanced high-loading (>3.5 mg cm⁻²) sulfur cathodes (Fig. 6g, Table S5). The desirable electrochemical performances of CoSA-N-C@S cathode pertaining to high sulfur loadings, high sulfur utilization, and high capacity retention corroborates that the CoSA-N-C could function as an advanced Li-S cathode

host because of the well-regulated polysulfide shuttling, propelled sulfur electrochemistry, as well as mediated lithium sulfide growth in the CoSA-N-C configurations.

3. Conclusions

In summary, by using a salt-template method, we have successfully fabricated CoSA-N-C with densely populated, monodispersed Co–N₄ coordinated moieties on a 2D nitrated carbon sheet as an advanced sulfur host material. Experimental and theoretical results demonstrate that the Co–N species not only help to chemically immobilize the soluble polysulfides, but also dynamically propel their fast conversion to insoluble end products (S or Li₂S), thereby eliminating the redox shuttling of polysulfides and the passivation of the Li metal anode. More importantly, the resultant CoSA-N-C achieves a homogeneous spatial distribution of Li₂S nanoparticles instead of traditional passivation layer, and subsequently catalyzes the oxidation of Li₂S into polysulfides, which is beneficial for high sulfur utilization. In addition, the wrinkled 2D morphology of CoSA-N-C together with numerous nanopores inside the nanosheets ensures smooth ions/mass transfer even at a 74.2 wt% sulfur content. With these multiple structural advantages, the CoSA-N-C@S electrode exhibits impressive electrochemical properties, including a large specific capacity of 1574 mAh·g⁻¹ at 0.05 C, a fading rate of 0.035% per cycle over 1000 cycles at 1 C, a high-rate capacity of 624 mAh g⁻¹ at 5 C, and an ultrahigh capacity retention of 91.8% after 120 cycles at 0.2 C with high sulfur loading of 4.9 mg cm⁻². The findings in the present study open inspiring opportunities in the rational design of high-loading single atomic metal catalysts that can synergistically regulate polysulfide electrocatalysis and lithium sulfide growth in Li–S batteries, the concepts of which can be extended to other energy conversion and storage systems.

Declaration of competing interest

The authors declare no competing financial interests.

CRediT authorship contribution statement

Yuanjian Li: Investigation, Data curation, Writing - original draft. **Jiabin Wu:** Investigation, Data curation, Methodology. **Bao Zhang:** Investigation, Data curation, Software. **Wenyu Wang:** Investigation. **Guoqun Zhang:** Investigation. **Zhi Wei Seh:** Investigation. **Nian Zhang:** Investigation. **Jie Sun:** Investigation. **Liang Huang:** Supervision, Methodology. **Jianjun Jiang:** Investigation. **Jun Zhou:** Investigation. **Yongming Sun:** Supervision, Conceptualization, Methodology, Writing - review & editing.

Acknowledgments

Y. S. acknowledges the financial support by the Innovation Fund of Wuhan National Laboratory for Optoelectronics of Huazhong University of Science and Technology. This work was financially supported by the National Natural Science Foundation of China (grants 51602115, 51972124). The authors would like to thank the Analytical and Testing Center of Huazhong University of Science and Technology as well as the Center for Nanoscale Characterization & Devices of Wuhan National Laboratory for Optoelectronics for providing the facilities to conduct the characterization. Z. W. S. acknowledges the support of the Singapore National Research Foundation (NRF-NRFF2017-04).

Appendix A. Supplementary data

Supplementary data to this article can be found online at <https://doi.org/10.1016/j.ensm.2020.05.022>.

References

- [1] P.G. Bruce, S.A. Freunberger, L.J. Hardwick, J.M. Tarascon, *Nat. Mater.* 11 (2012) 2.
- [2] Y. Sun, N. Liu, Y. Cui, *Nat. Energy* 1 (2016) 16071.
- [3] Y. Yuan, J. Lu, *Carbon Energy* 1 (2019) 8–12.
- [4] Y. Cao, M. Li, J. Lu, J. Liu, K. Amine, *Nat. Nanotechnol.* 14 (2019) 200–207.
- [5] Z.W. Seh, Y. Sun, Q. Zhang, Y. Cui, *Chem. Soc. Rev.* 45 (2016) 5605–5634.
- [6] M. Liu, X. Qin, Y.-B. He, B. Li, F. Kang, *J. Mater. Chem. A* 5 (2017) 5222.
- [7] A. Manthiram, Y. Fu, S.H. Chung, C. Zu, Y.S. Su, *Chem. Rev.* 114 (2014) 11751–11787.
- [8] H. Wang, Y. Cui, *Carbon Energy* 1 (2019) 13–18.
- [9] S. Tu, X. Chen, X. Zhao, M. Cheng, P. Xiong, Y. He, Q. Zhang, Y. Xu, *Adv. Mater.* 30 (2018) 1804581.
- [10] Y. Chen, A. Elangovan, D. Zeng, Y. Zhang, H. Ke, J. Li, Y. Sun, H. Cheng, *Adv. Funct. Mater.* 29 (2019) 1906444.
- [11] H. Pan, J. Chen, R. Cao, V. Murugesan, N.N. Rajput, K.S. Han, K. Persson, L. Estevez, M.H. Engelhard, J.-G. Zhang, K.T. Mueller, Y. Cui, Y. Shao, J. Liu, *Nat. Energy* 2 (2017) 813.
- [12] W. Xue, Z. Shi, L. Suo, C. Wang, Z. Wang, H. Wang, K.P. So, A. Maurano, D. Yu, Y. Chen, L. Qie, Z. Zhu, G. Xu, J. Kong, J. Li, *Nat. Energy* 4 (2019) 374–382.
- [13] M. Liu, Q. Li, X. Qin, G. Liang, W. Han, D. Zhou, Y.-B. He, B. Li, F. Kang, *Small* 13 (2017) 131602539.
- [14] Y. Li, W. Wang, X. Liu, E. Mao, M. Wan, G. Li, L. Fu, Z. Li, A.Y.S. Eng, Z.W. Seh, Y. Sun, *Energy Storage Mater.* 23 (2019) 261–268.
- [15] W. Shin, J. Lu, X. Ji, *Carbon Energy* 1 (2019) 165–172.
- [16] G. Zhou, K. Liu, Y. Fan, M. Yuan, B. Liu, W. Liu, F. Shi, Y. Liu, W. Chen, J. Lopez, D. Zhuo, J. Zhao, Y. Tsao, X. Huang, Q. Zhang, Y. Cui, *ACS Cent. Sci.* 4 (2018) 260.
- [17] Y. Pan, Y. Zhou, Q. Zhao, Y. Dou, S. Chou, F. Cheng, J. Chen, H.K. Liu, L. Jiang, S.X. Dou, *Nano Energy* 33 (2017) 205–212.
- [18] M. Liu, D. Zhou, Y.-B. He, Y. Fu, X. Qina, C. Miao, H. Du, B. Li, Q.-H. Yang, Z. Lin, T.S. Zhao, F. Kang, *Nano Energy* 22 (2016) 278–289.
- [19] Q. Pang, A. Shyamsunder, B. Narayanan, C.Y. Kwok, L.A. Curtiss, L.F. Nazar, *Nat. Energy* 3 (2018) 783.
- [20] X. Ji, K.T. Lee, L.F. Nazar, *Nat. Mater.* 8 (2009) 500.
- [21] F. Pei, L. Lin, D. Ou, Z. Zheng, S. Mo, X. Fang, N. Zheng, *Nat. Commun.* 8 (2017) 482.
- [22] L. Du, Q. Wu, L. Yang, X. Wang, R. Che, Z. Lyu, W. Chen, X. Wang, Z. Hu, *Nano Energy* 57 (2019) 34–40.
- [23] Z.W. Seh, W. Li, J.J. Cha, G. Zheng, Y. Yang, M.T. McDowell, P.C. Hsu, Y. Cui, *Nat. Commun.* 4 (2013) 1331.
- [24] X. Liang, C. Hart, Q. Pang, A. Garsuch, T. Weiss, L.F. Nazar, *Nat. Commun.* 6 (2015) 5682.
- [25] Z. Li, J. Zhang, B. Guan, D. Wang, L.M. Liu, X.W. Lou, *Nat. Commun.* 7 (2016) 13065.
- [26] H.J. Peng, G. Zhang, X. Chen, Z.W. Zhang, W.T. Xu, J.Q. Huang, Q. Zhang, *Angew. Chem. Int. Ed.* 55 (2016) 12990.
- [27] R. Wang, J. Yang, X. Chen, Y. Zhao, W. Zhao, G. Qian, S. Li, Y. Xiao, H. Chen, Y. Ye, G.M. Zhou, F. Pan, *Adv. Mater.* 32 (2020) 1903350.
- [28] L. Ma, W. Zhang, L. Wang, Y. Hu, G. Zhu, Y. Wang, R. Chen, T. Chen, Z. Tie, J. Liu, Z. Jin, *ACS Nano* 12 (2018) 4868.
- [29] G. Zhou, H. Tian, Y. Jin, X. Tao, B. Liu, R. Zhang, Z.W. Seh, D. Zhuo, Y. Liu, J. Sun, J. Zhao, C. Zu, S. Wu, Q. Zhang, Y. Cui, *Proc. Natl. Acad. Sci. U. S. A.* 114 (2017) 840.
- [30] Y. Tsao, M. Lee, E.C. Miller, G. Gao, J. Park, S. Chen, T. Katsumata, H. Tran, L.-W. Wang, M.F. Toney, Y. Cui, Z. Bao, *Joule* 3 (2019) 872.
- [31] Y. Fu, Z. Wu, Y. Yuan, P. Chen, L. Yu, L. Yuan, Q. Han, Y. Lan, W. Bai, E. Kan, C. Huang, X. Ouyang, X. Wang, J. Zhu, J. Lu, *Nat. Commun.* 11 (2020) 845.
- [32] H.A. Salem, G. Babu, C.V. Rao, L.M. Arava, *J. Am. Chem. Soc.* 137 (2015) 11542.
- [33] D. Fang, Y. Wang, C. Qian, X. Liu, X. Wang, S. Chen, S. Zhang, *Adv. Funct. Mater.* 29 (2019) 1900875.
- [34] Y. Li, C. Wang, W. Wang, A.Y.S. Eng, M. Wan, L. Fu, E. Mao, G. Li, J. Tang, Z.W. Seh, Y. Sun, *ACS Nano* 14 (2020) 1148–1157.
- [35] Z. Yuan, H.J. Peng, T.Z. Hou, J.-Q. Huang, C.M. Chen, D.W. Wang, X.B. Cheng, F. Wei, Q. Zhang, *Nano Lett.* 16 (2016) 519.
- [36] Y. Zhong, L. Yin, P. He, W. Liu, Z. Wu, H. Wang, *J. Am. Chem. Soc.* 140 (2018) 1455.
- [37] Q. Pang, C.Y. Kwok, D. Kundu, X. Liang, L.F. Nazar, *Joule* 3 (2019) 1.
- [38] J. Wu, L. Xiong, B. Zhao, M. Liu, L. Huang, *Small Methods* 4 (2020) 1900540.
- [39] B.W. Zhang, T. Sheng, Y.D. Liu, Y.X. Wang, L. Zhang, W.H. Lai, L. Wang, J. Yang, Q.F. Gu, S.L. Chou, H.K. Liu, S.X. Dou, *Nat. Commun.* 9 (2018) 4082.
- [40] Z. Du, X. Chen, W. Hu, C. Chuang, S. Xie, A. Hu, W. Yan, X. Kong, X. Wu, H. Ji, L.-J. Wan, *J. Am. Chem. Soc.* 141 (2019) 3977.
- [41] Z. Liu, L. Zhou, Q. Ge, R. Chen, M. Ni, W. Utetiwo, X. Zhang, W. Yang, *ACS Appl. Mater. Interfaces* 10 (2018) 19311.
- [42] J. Wang, L. Jia, J. Zhong, Q. Xiao, C. Wang, K. Zang, H. Liu, H. Zheng, J. Luo, J. Yang, H. Fan, W. Duan, Y. Wu, H. Lin, Y. Zhang, *Energy Storage Mater.* 18 (2019) 246.
- [43] K. Zhang, Z. Chen, R. Ning, S. Xi, W. Tang, Y. Du, C. Liu, Z. Ren, X. Chi, M. Bai, C. Shen, X. Li, X. Wang, X. Zhao, K. Leng, S.J. Pennycook, H. Li, H. Xu, K.P. Loh, K. Xie, *ACS Appl. Mater. Interfaces* 11 (2019) 25147.
- [44] B.-Q. Li, L. Kong, C.-X. Zhao, Q. Jin, X. Chen, H.-J. Peng, J.-L. Qin, J.-X. Chen, H. Yuan, Q. Zhang, J.-Q. Huang, *InfoMat* 1 (2019) 533–541.
- [45] J. Wu, J. Chen, Y. Huang, K. Feng, J. Deng, W. Huang, Y. Wu, J. Zhong, Y. Li, *Sci. Bull.* 64 (2019) 1875–1880.

- [46] L. Zhang, D. Liu, Z. Muhammad, F. Wan, W. Xie, Y. Wang, L. Song, Z. Niu, J. Chen, *Adv. Mater.* 31 (2019) 1903955.
- [47] G. Zhou, S. Zhao, T. Wang, S.Z. Yang, B. Johannessen, H. Chen, C. Liu, Y. Ye, Y. Wu, Y. Peng, C. Liu, S.P. Jiang, Q. Zhang, Y. Cui, *Nano Lett.* 20 (2020) 1252–1261.
- [48] J. Xie, B.-Q. Li, H.-J. Peng, Y.-W. Song, M. Zhao, X. Chen, Q. Zhang, J.-Q. Huang, *Adv. Mater.* 31 (2019) 1903813.
- [49] Y. Li, P. Zhou, H. Li, T. Gao, L. Zhou, Y. Zhang, N. Xiao, Z. Xia, L. Wang, Q. Zhang, L. Gu, S. Guo, *Small Methods* 4 (2020) 1900701.
- [50] Y. Song, W. Zhao, L. Kong, L. Zhang, X. Zhu, Y. Shao, F. Ding, Q. Zhang, J. Sun, Z. Liu, *Energy Environ. Sci.* 11 (2018) 2620.
- [51] T. Zhou, W. Lv, J. Li, G. Zhou, Y. Zhao, S. Fan, B. Liu, B. Li, F. Kang, Q.-H. Yang, *Energy Environ. Sci.* 10 (2017) 1694.
- [52] F.Y. Fan, W.C. Carter, Y.-M. Chiang, *Adv. Mater.* 27 (2015) 5203.
- [53] J. Wu, H. Zhou, Q. Li, M. Chen, J. Wan, N. Zhang, L. Xiong, S. Li, B. Xia, G. Feng, M. Liu, L. Huang, *Adv. Energy Mater.* 9 (2019) 1900149.
- [54] Y.-J. Li, J.-M. Fan, M.-S. Zheng, Q.-F. Dong, *Energy Environ. Sci.* 9 (2016) 1998.
- [55] C. He, C. Yang, J. Yang, N. Han, R. Yuan, Y. Chen, H. Liu, T. Xie, R. Chen, H. Zhou, W. Liu, X. Sun, *ACS Appl. Energy Mater.* 2 (2019) 2904.
- [56] G. Li, W. Lei, D. Luo, Y. Deng, Z. Deng, D. Wang, A. Yu, Z. Chen, *Energy Environ. Sci.* 11 (2018) 2372.
- [57] X. Yu, J. Deng, R. Lv, Z.-H. Huang, B. Li, F. Kang, *Energy Storage Mater.* 20 (2019) 14.
- [58] W. Huang, Z. Lin, H. Liu, R. Na, J. Tian, Z. Shan, *J. Mater. Chem. A* 6 (2018) 17132.
- [59] Q. Wu, X. Zhou, J. Xu, F. Cao, C. Li, *ACS Nano* 13 (2019) 9520.
- [60] H. Lin, L. Yang, X. Jiang, G. Li, T. Zhang, Q. Yao, G. Zheng, J.Y. Lee, *Energy Environ. Sci.* 10 (2017) 1476.
- [61] H. Lin, S. Zhang, T. Zhang, H. Ye, Q. Yao, G. Zheng, J.Y. Lee, *Adv. Energy Mater.* 9 (2019) 1902096.
- [62] W.G. Lim, Y. Mun, A. Cho, C. Jo, S. Lee, J.W. Han, J. Lee, *ACS Nano* 12 (2018) 6013.
- [63] H. Lin, S. Zhang, T. Zhang, S. Gao, H. Ye, Q. Yao, G. Zheng, J.Y. Lee, *ACS Nano* 13 (2019) 7073.
- [64] J. He, G. Hartmann, M. Lee, G.S. Hwang, Y. Chen, A. Manthiram, *Energy Environ. Sci.* 12 (2019) 344–350.
- [65] M. Yu, S. Zhou, Z. Wang, Y. Wang, N. Zhang, S. Wang, J. Zhao, J. Qiu, *Energy Storage Mater.* 20 (2019) 98.
- [66] X. Huang, J. Tang, B. Luo, R. Knibbe, T. Lin, H. Hu, M. Rana, Y. Hu, X. Zhu, Q. Gu, D. Wang, L. Zhou, *Adv. Energy Mater.* 9 (2019) 1901872.
- [67] M. Wang, Y. Song, Z. Sun, Y. Shao, C. Wei, Z. Xia, Z. Tian, Z. Liu, J. Sun, *ACS Nano* 13 (2019) 13235–13243.
- [68] H. Yuan, H.-J. Peng, B.-Q. Li, J. Xie, L. Kong, M. Zhao, X. Chen, J.-Q. Huang, Q. Zhang, *Adv. Energy Mater.* 9 (2019) 1802768.
- [69] Z. Ye, Y. Jiang, J. Qian, W. Li, T. Feng, L. Li, F. Wu, R. Chen, *Nano Energy* 64 (2019) 103965.